unreinforced material for all values of $\Delta\varepsilon_p/2$ owing to its higher monotonic strength.

4. Cyclic deformation: mechanical effects

4.1. Micromechanical modelling

It is evident that the mechanical behavior of DRC not only depends on the changes in the matrix microstructure but also on the load transfer from the ductile matrix to the rigid reinforcements. This process can be studied through micromechanical models based on continuum mechanics. Two different approaches were used to analyze this problem. The first is based on the mean-field theories, which represent the stresses and strains in each phase by means of volume-averaged quantities. They have been extensively used to model the monotonic deformation of DRC (see, for instance, [63–66] and references therein) but their application to problems involving forward and reverse deformation was limited [63,67,68]. The second type of simulation was based on the finite element analysis of a periodic unit cell, representative of the composite [69–75]. These models were more extensively used to study the Bauschinger effect, fully-reversed cyclic deformation, and thermo-mechanical fatigue [45,50,76–80]. They are widely exploited in this review to illustrate the reinforcement/matrix interaction upon cyclic loading. Moreover, these latter models provide the local stress and strain fields in each material and at the matrix–reinforcement interface, magnitudes necessary to account for the development of damage during deformation.

The unit cell analyses are based on the spatial representation shown in Fig. 8, where the material was idealized as a three-dimensional array of hexagonal prisms. The ceramic reinforcements were located at the center of each prism and their shape was either spherical or cylindrical, the cylinder axis being parallel to the prism axis. Reinforcements of three different shapes were studied: spheres are adequate to model equiaxed reinforcements of rounded shape; short cylinders (whose height is equal to the diameter), a good approximation of particles with irregular shape, sharp corners and low aspect ratio; and long cylinders with a length to diameter aspect ratio of 5 representing whiskers [69–73]. The aspect ratio of the hexagonal prism was equal to that of the reinforcement (1 for spheres and short cylinders and five for whiskers).

As proposed by Tvergaard [81], the behavior of the hexagonal prisms can be approximated through the finite element analysis of axisymmetric cylindrical cells (Fig. 8). Due to the symmetries of the problem, only one half of the cylindrical cell needs to be analyzed. The finite element discretizations for the three reinforcement shapes (spheres, unit cylinders or particles, and long cylinders or whiskers) are shown in Figs. 9(a)–(c), respectively, for the cells containing 20 vol.% of reinforcement. Attention was confined to axisymmetric deformations, so all field quantities are solely functions of r and z, and symmetry was assumed for the r and z axes within each cell. In addition, the circular cylindrical cell was required to remain

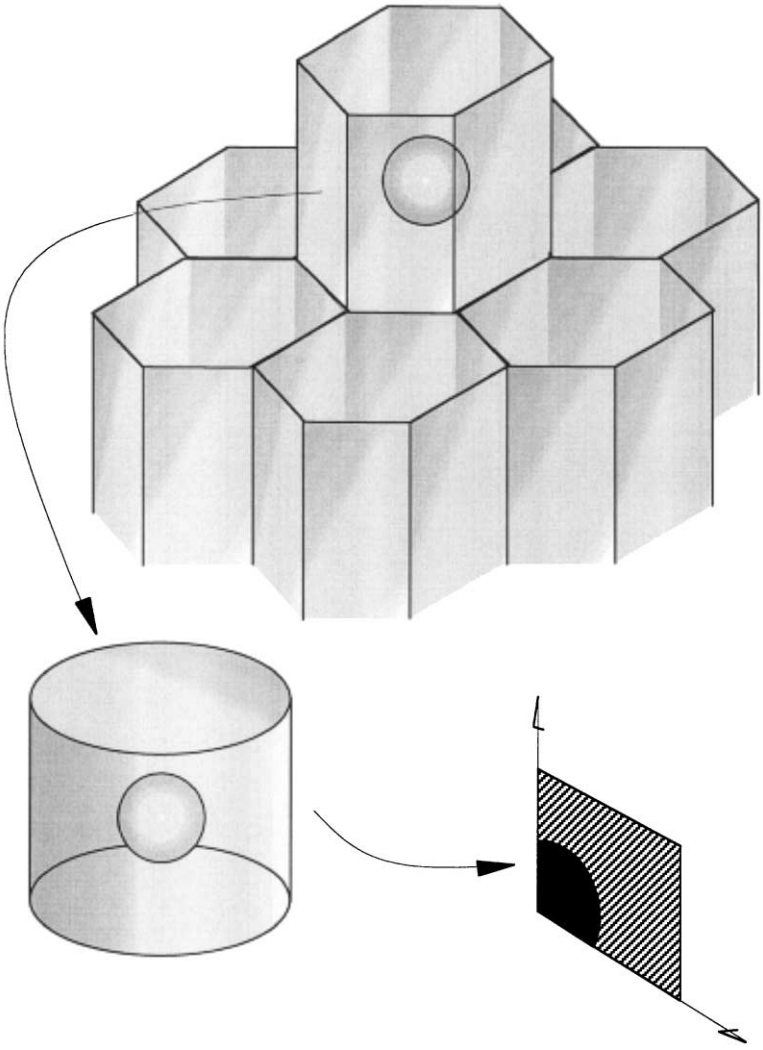

Fig. 8. Composite idealization as a three-dimensional array of hexagonal prisms, each containing a spherical reinforcement at the center.

cylindrical during deformation to ensure the displacement compatibility between neighbor hexagonal prisms. Thus the straight lines bounding each cell must remain straight during the analysis and form right angles. The matrix and the reinforcement were considered to be perfectly bonded by assuring the displacement continuity across the interface. Details on the numerical technique and the precise boundary conditions can be found elsewhere [79].

The uniaxial stress–strain response ($\sigma-\epsilon$) of the composite in the z direction can be computed from the unit cell behaviour according to

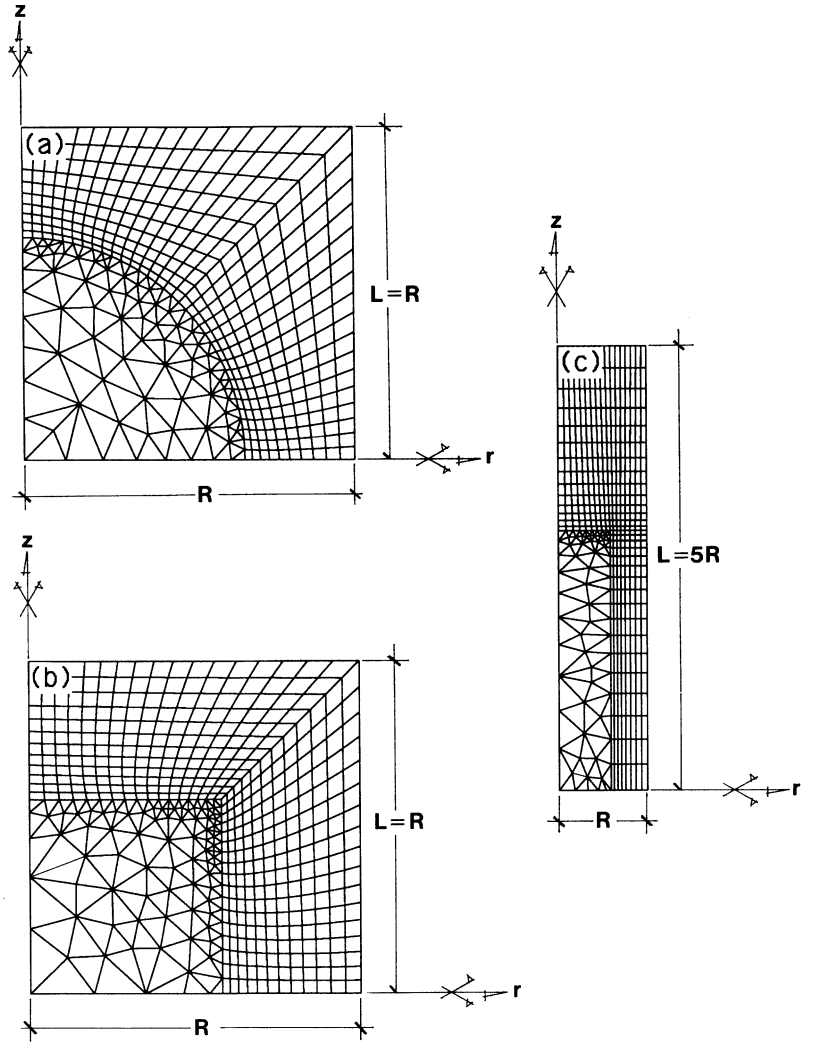

Fig. 9. Finite element discretization of the axisymmetric unit cells for a 20 vol.% of reinforcement: (a) spheres; (b) particles (short cylinders); (c) whiskers (long cylinders).

$$\epsilon = \ln(1 + U/L) \quad \text{and} \quad \sigma = \frac{1}{\Omega}\int_{\Omega} T_z \mathrm{d}\Omega \tag{2}$$

where U and T_z, stand, respectively, for a uniform displacement and the corresponding stresses on the upper boundary of the unit cell, both in the z direction, while Ω stands for the current area of the cell face with normal in the same direction. The ceramic reinforcements were assumed to behave as isotropic linear elastic materials. The matrix behavior was represented by an elasto-plastic solid with isotropic hardening following the incremental theory of plasticity. Parameters representative of

commercial high strength Al alloys reinforced with SiC particles or whiskers were used in the numerical simulations.

4.2. The Bauschinger effect

The mechanical response under fully reversed deformation was obtained by applying an alternating displacement $\pm U$ to the upper boundary of the unit cell. The stress–strain behavior during ten loading cycles at $\Delta\varepsilon/2 = 1\%$ is plotted in Fig. 10(a) for the composite reinforced with 20 vol.% SiC particles. This plot reveals the presence of a Bauschinger effect, which should be an intrinsic composite effect because the matrix isotropic hardening rule for the plastic flow cannot take account of this behavior. The existence of a Bauschinger effect in particle- and fiber-reinforced metallic alloys, well documented experimentally [82–85], was rationalized as follows. Two important contributions to strengthening in these materials during forward deformation were identified: (i) a homogeneous mean stress in the matrix produced by Orowan loops formed by the dislocations around the ceramic particles during plastic flow. This mean stress opposes continued forward deformation during monotonic loading, thereby causing work hardening. (ii) An additional inhomogeneous stress in the vicinity of the particles (''source-shortening stress'') created by the Orowan loops because their presence around the particles repels successive dislocations. Upon reverse deformation, the Bauschinger effect was a result of the removal of Orowan loops by the formation of secondary dislocations and prismatic loops of primary Burgers vectors [82] or by the shrinkage of Orowan loops by climb through pipe diffusion [83].

The influence of dislocation/particle interactions on the Bauschinger effect should be preponderant when the particles and the interparticle distance are of the other of 1 μm or below. Both magnitudes are higher in DRC, and the numerical simulations point out an additional source of the Bauschinger effect in these composites [76]. Plastic strains appear along the reinforcement–matrix interface during monotonic loading, especially around the particle and whisker sharp corners, due to the differences between the mechanical properties of the matrix and reinforcement. The matrix plastic deformation is constrained by the presence of the brittle reinforcements, and large hydrostatic stresses develop in the matrix, increasing significantly the composite flow stress. Both the inhomogeneous plastic strain field in the matrix and the hydrostatic stresses lead to the development of the Bauschinger effect in the composite upon reversed deformation.

Systematic numerical simulations [69,70,73] have shown that the triaxiality levels in the matrix increase with the applied strain and the reinforcement volume fraction, and that they are highly dependent on the reinforcement shape and spatial distribution. In particular, whiskers oriented in the loading axis lead to much higher hydrostatic stresses in the matrix than either spherical or irregular particles of equiaxed shape. The experimental data in DRC are in agreement with these observations: the Bauschinger stress[2] increased with the amount of forward deformation [67,86,87], and was greater for whisker-reinforced composites than for particle-

[2] The Bauschinger stress is the difference between the forward and reversed yield stress in a Bauschinger test and expresses the softening induced in the material when the direction of load is reversed.

reinforced ones [86]. The experiments also revealed that the Bauschinger effect was more marked if the composite was initially deformed in compression [86,87]. This was explained in terms of the thermal residual stresses which develop in the com-

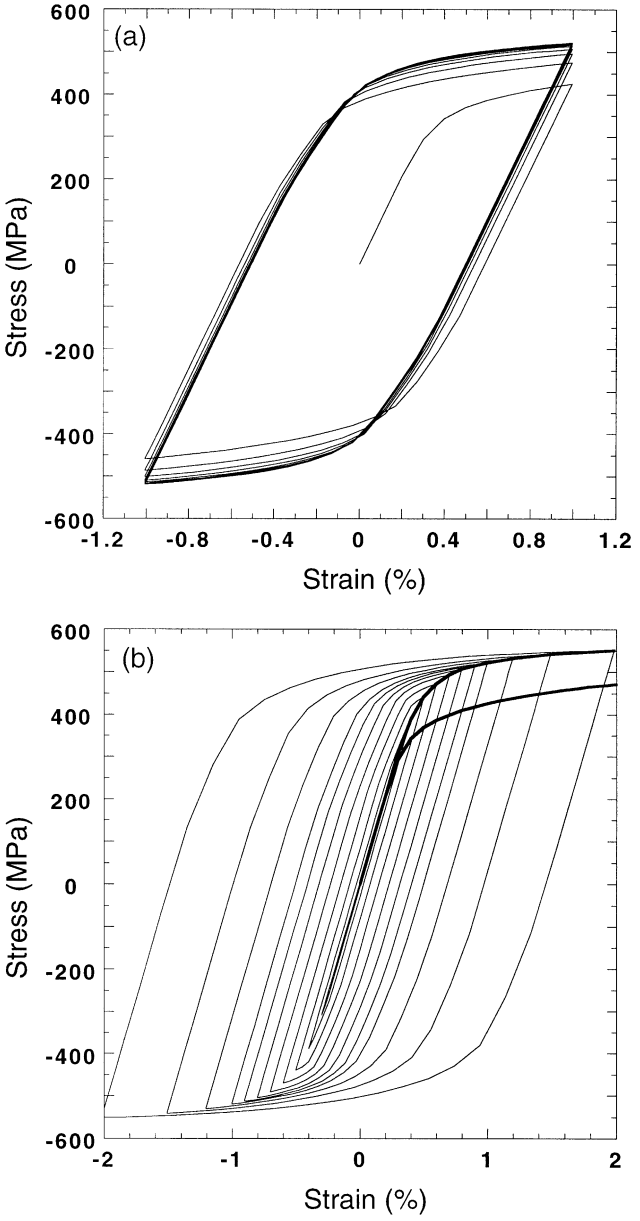

Fig. 10. DRC containing 20 vol.% of SiC particles: (a) stress–strain behavior during 10 cycles at $\Delta\varepsilon/2 = 1\%$; (b) saturated hysteresis 1oops at various $\Delta\varepsilon/2$. The monotonic and cyclic (saturated) stress–strain curves (thick lines) are also plotted (reprinted by permission of Elsevier from [78]).

posite upon cooling as a result of the thermal expansion mismatch between the metallic matrix and the ceramic reinforcements [77]. Tensile residual stresses appear in the matrix and this increases the compressive yield strength of the composite and reduces the tensile one, affecting the corresponding values of the Bauschinger stress.

4.3. Fully-reversed deformation

The stress-strain behavior under fully reversed cyclic deformation in Fig. 10(a) shows that the material hardened very quickly during the first cycles. The hardening rate then decreased progressively, and a saturated hysteresis loop was eventually attained. A similar behavior was found in the range $0{,}1\% \leqslant \Delta\epsilon/2 \leqslant 2.0\%$ and the saturated hysteresis loops are plotted in Fig. 10(b). The cyclic stress–strain curve was then obtained by drawing a line through the tips of the saturated hysteresis loops, plotted in Fig. 10(b) together with the monotonic stress–strain curve. The mechanisms of cyclic strain hardening in the composite can be readily understood if the isolines of constant effective plastic strain, ϵ_p, in the matrix are plotted after one, three and ten loading cycles at $\Delta\varepsilon/2 = 1.0\%$ when the far-field applied strain, ϵ, was 1.0% (Fig. 11). Plastic strains developed around the particle sharp corner during monotonic deformation in the first cycle. However, the plastic strains did not cover the entire unit cell, and their magnitude is not very high, the maximum value being close to 0.05 (Fig. 11a). After three loading cycles, the plastic strains reached 0.2 around the particle corner, and plastic strains in excess of 0.05 covered most of the unit cell (Fig. 11b). This build-up of plastic strains continued upon further loading and unloading, and plastic strains over 0.2 were spread throughout the matrix after 10 loading cycles [Fig. 11(c)].

The increase in the composite flow resistance reflects the strain hardening of the matrix due to the progressive accumulation of plastic deformations in each loading cycle. The matrix strain hardening capacity is higher at low strains, and thus the composite hardened very quickly in the first cycles, as was found experimentally [44-54]. In addition, the numerical simulations explain the qualitative differences in cyclic hardening between the underaged and peak-aged composites [55]. The matrix in the former exhibits a very low yield strength followed by a large strain hardening capacity. This leads to a marked cyclic hardening as the plastic strains build up in the matrix upon cyclic deformation. On the contrary, the matrix in peak-aged materials presents very high yield strength but the flow stress remains practically constant afterwards. As a result, the accumulation of plastic strain does not lead to significant hardening.

One important difference between the monotonic and cyclic hardening mechanisms in DRC is found in the role played by the hydrostatic stresses. The isolines of constant hydrostatic stress, σ_h are shown in Fig. 12 after one and ten cycles at $\Delta\varepsilon/2 = 1.0\%$ when the far-field applied strain, ϵ, was 1.0%. The increment in the triaxiality levels in the matrix was very limited during cyclic loading, so the contribution of this factor to the cyclic hardening seemed to be less important than the build-up of plastic strains in the matrix. This is the opposite of monotonic

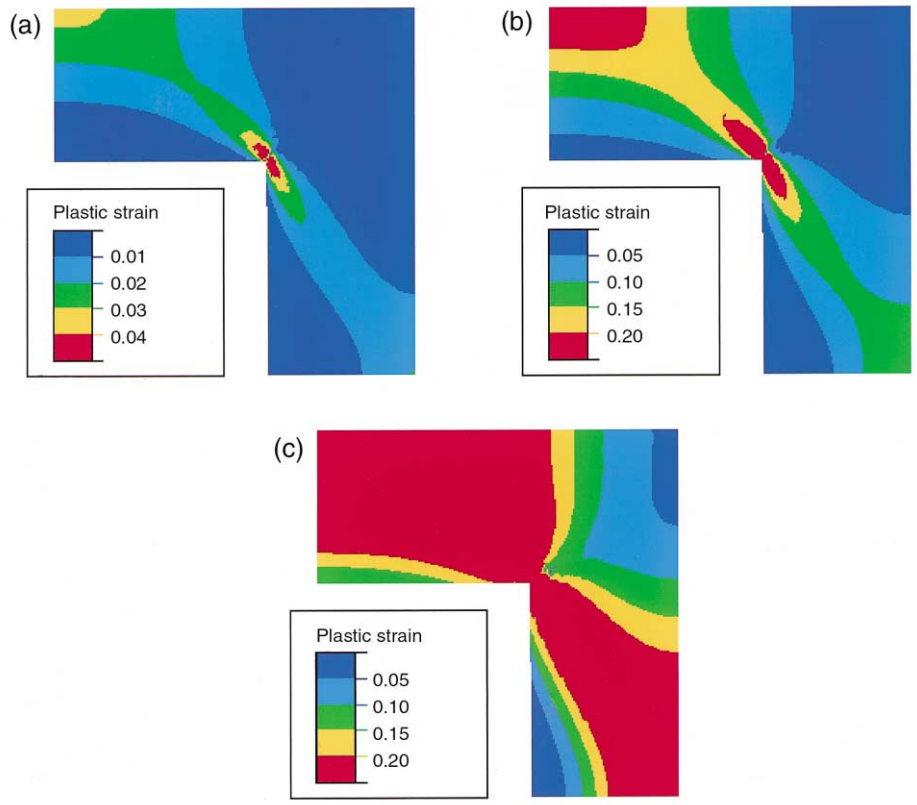

Fig. 11. DRC containing 20 vol.% of SiC particles. Isolines of constant effective plastic strain in the matrix, ε_p after (a) one (monotonic); (b) three; (c) and ten loading cycles at $\Delta\varepsilon/2 = 1.0\%$ when the far-field applied strain, ε, was 1.0% (reprinted by permission of Elsevier from [78]).

deformation, where the effect of hydrostratic stresses in the composite strength was dominant from the continuum mechanics viewpoint. As a result, reinforcement volume fraction and shape are expected to be secondary factors—as compared to the matrix hardening capacity—to determine the cyclic hardening under fully reversed deformation. This is shown in Fig. 13 where the monotonic and cyclic stress-strain curves are plotted for three DRC containing 20 vol.% of spheres, unit cylinders (particles) or long cylinders (whiskers). The stresses are normalized by σ_0, the initial yield stress of the matrix. The monotonic stress–strain curve of the matrix can also be found. The strengthening provided by the spheres upon monotonic deformation was small as compared with that of the particles, and both significantly lower than that obtained through whisker reinforcement. However, the cyclic hardening—which is the difference between the solid and dashed curve for each composite—was very close in all three cases. Similar results were obtained for DRC reinforced with different volume fractions of the same reinforcement [78] although for the sake of brevity they are not plotted here.

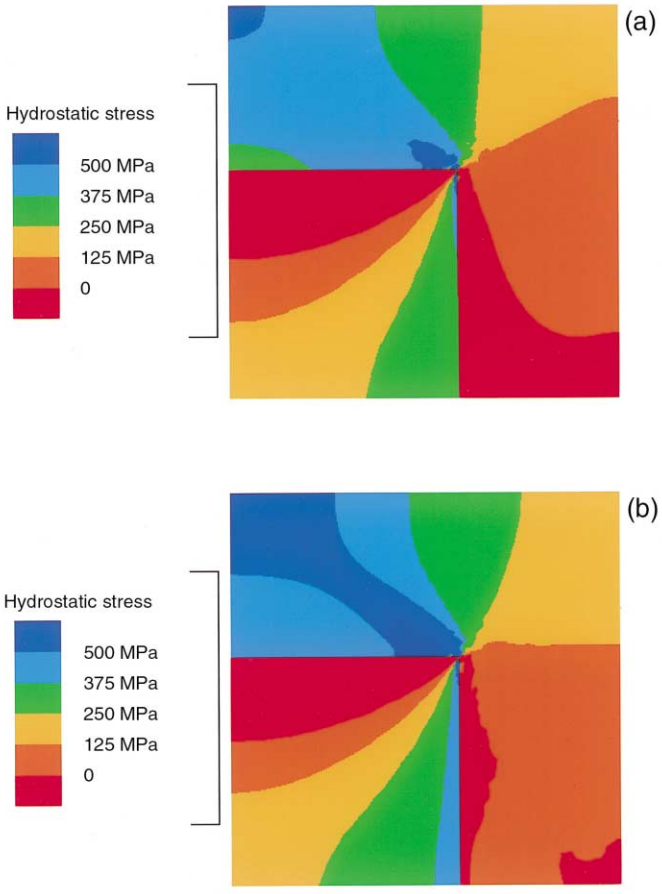

Fig. 12. DRC containing 20 vol.% of SiC particles. Isolines of constant hydrostatic stress, σ_h, after (a) one (monotonic); (b) 10 loading cycles at $\Delta\varepsilon/2 = 1.0\%$ when the far-field applied strain, ε, was 1.0% (reprinted by permission of Elsevier from [78]).

4.4. Thermo-mechanical deformation

Thermal residual stresses are always present in these composites and induce an asymmetry during the initial stress–strain loops. They are, however, rapidly smoothed out as the plastic strain is spread through the matrix during cyclic deformation [88–90] and their effect on the overall cyclic stress–strain behavior is not important. This is not the case with thermo-mechanical fatigue loading, where thermal and mechanical cyclic strains are applied simultaneously to the material. Thermal strains are erased rapidly during pure mechanical loading but are generated in each fatigue cycle upon thermomechanical fatigue. Two kinds of thermo-mechanical loading may be distinguished, depending on the synchronization of the thermal and mechanical strains: the maximum (tensile) mechanical stresses coincide

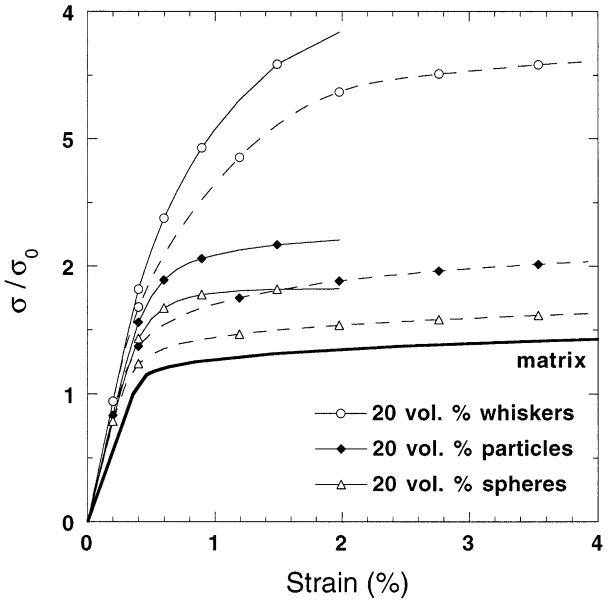

Fig. 13. Monotonic (dashed lines) and cyclic (solid lines) stress–strain curves for composites reinforced with 20 vol.% of either whiskers, particles or spheres. The monotonic stress–strain curve of the matrix is also shown. The stresses are normalized by the matrix initial yield stress, σ_0 (reprinted by permission of Elsevier from [78]).

with the maximum temperature in the cycle during in-phase loading, while the maximum temperature is attained when the mechanical stresses are minimum (compressive) for out-of-phase loading.

The stress evolution in each phase during thermo-mechanical fatigue was determined by Karayaka and Sehitoglu through a mean-field approach for in-phase and out-of-phase loading [68]. In the absence of thermal strains, the sign of the hydrostatic component of the matrix stresses is equal to that of the external load: positive in the tensile part of the fatigue cycle and negative otherwise. However, the mismatch between matrix and reinforcement thermal expansion coefficients induces negative hydrostatic stresses in the matrix upon heating, which are reversed upon cooling. They are subtracted from the mechanical stresses during in-phase loading and added to them for out-phase deformation. Evidently, the influence of the thermal strains increases with the reinforcement volume fraction and with the difference between the maximum and minimum temperature in the cycle. Their effect on the overall behavior of the composite is discussed in Section 7.3.

5. Fatigue damage and crack nucleation

Fatigue failure of metallic materials is induced by the nucleation of one or several microcracks which propagate slowly during cyclic loading until one of them reaches

the critical size and catastrophic failure occurs. It is well known that the nucleation phase takes up to 90% of the fatigue life in the high cycle fatigue regime, and in addition, the fatigue limit of smooth specimens is often determined by the ability of nucleating a crack from microstructural inhomogeneities and surface defects [36]. This section of the review is devoted to present the micromechanisms of fatigue crack nucleation in DRC and begins by analyzing the progression of damage during fatigue in these composites.

5.1. Damage upon cyclic loading

The experimental evidence of the progressive development of damage during cyclic deformation in DRC is limited to a few investigations. For instance, Li and Ellyin [91] used periodic surface replication of smooth specimens with a shallow notch, while Llorca and co-workers [48,50,53,54] cut the broken specimens through the middle along the loading direction and examined the longitudinal sections under the microscope. They found that damage was initially generated randomly throughout the specimens, and the dominant damage micromechanisms detected at this stage were reinforcement fracture [48,50,53,54,91], decohesion at the matrix/reinforcement interface [51,54,91], and the formation of matrix cracks [51]. This situation of homogeneous damage continued until a dominant microcrack was nucleated at the specimen surface, and damage was then rapidly localized around the propagating crack.

The broken reinforcements were usually fractured by cracks perpendicular to the loading axis (Fig. 14(a)]. This failure mechanism is normal in DRC tested in tension [92,93] and this indicated that the ceramic particles were fractured during the tensile part of the fatigue cycle. As in the specimens tested in tension, the fracture probability increased with reinforcement size because the strength of brittle ceramic reinforcements follows the Weibull statistics. In addition, elongated reinforcements oriented in the loaded direction were more prone to fail than equiaxed ones. All studies reported that particle clusters, where the local volume fraction of reinforcements is very high, were preferential sites for damage nucleation [53,54,91].

Ceramic particles broken by cracks parallel to the loading axis were also found in two Al-matrix composites reinforced with alumina particles [48]. Their fracture morphology was similar to that found in DRC tested in compression [94], and is representative of particles broken by splitting during the compressive part of the fatigue cycle. Their volume fraction was, however, very small and they were not found in other DRC tested in similar conditions.

Damage by interface decohesion and matrix cracking was also observed throughout the specimen in other DRC composites. They were mainly concentrated at or near the ends of elongated reinforcements and whiskers [51,54,91] but no influence was found of the reinforcement size in the failure probability. In addition, decohesion was often observed in particle clusters and this was partially attributed to the difficulties to infiltrate the matrix in these regions, which led to poor interfacial bonding.

The progression of damage during cyclic deformation can be readily understood from the results of the unit cell analyses presented in Section 4. In particular, the

evolution of the average stress at the center of a unit cylinder is plotted in Fig. l4(b) as a function of the applied strain [50]. The matrix and reinforcement properties correspond to the materials presented in Figs. 10–12. This plot shows that the

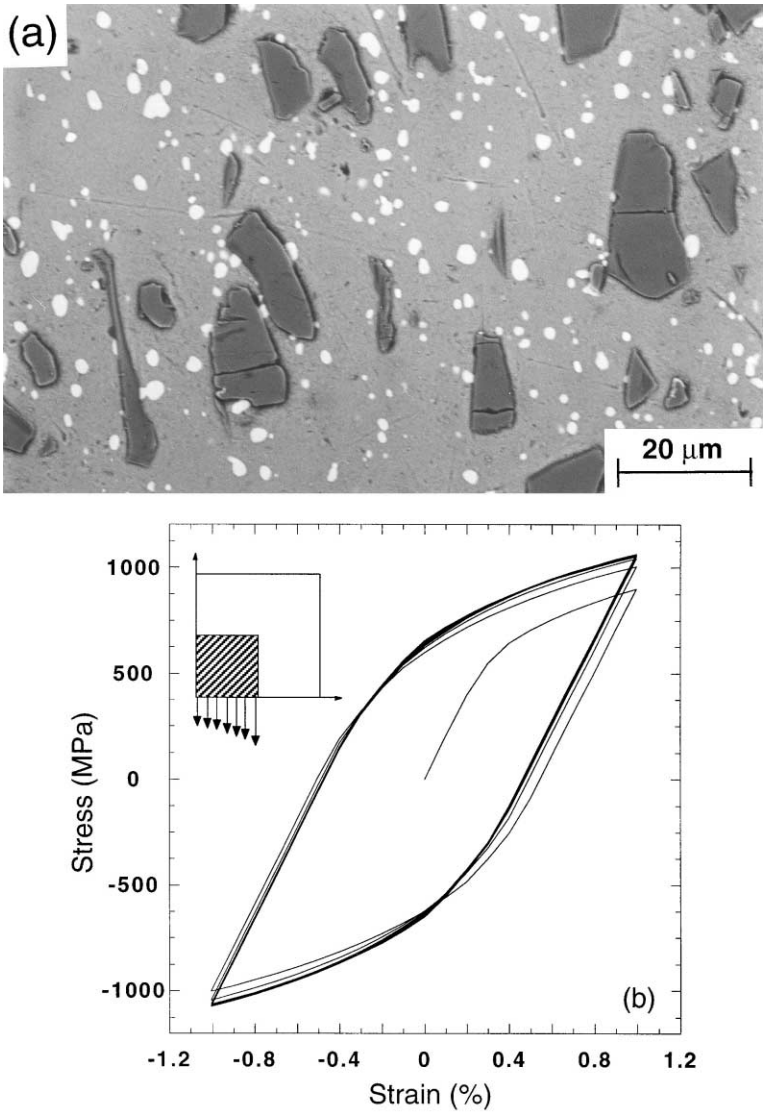

Fig. 14. (a) Back-scattered scanning electron micrograph showing SiC particles broken during cyclic deformation far away from the fracture surface in a 2618 Al alloy reinforced with 15 vol.% SiC particles. The white regions are Al_9NiFe intermetallic inclusions. Loading axis was vertical (reprinted by permission of Elsevier from [50]). (b) Evolution of the average stress at the center of the particle as a function of the applied strain during cyclic deformation. The composite properties and loading conditions correspond to those presented in Figs. 11 and 12.

stresses transferred from the matrix to the particles increased during cyclic loading as a result of the cyclic hardening of the matrix. Similar results are found if the normal stresses at the particle/matrix interface are plotted versus the applied strain. These simulations demonstrate that the stresses acting on the reinforcements and on the interface increased progressively during cyclic loading thus increasing the number of damaged particles.

Llorca [78] carried out a parametric study of the effect of reinforcement volume fraction and shape on the average stress acting on the reinforcements and at the interface upon cyclic deformation. His simulations were in agreement with many of the experimental findings of damage nucleation reported above. In particular, the average stresses in the reinforcements and at the reinforcement ends were higher for elongated particles oriented in the loading direction than for equiaxed ones. In addition, reinforcement and interface stresses increased with the reinforcement volume fraction, supporting the higher damage nucleation probability found in clusters. Finally, the unit cell simulations showed that the reinforcement and interface stresses increased rapidly with the cyclic strain amplitude. Thus, very little damage is expected to occur far away from the fatigue fracture surface under high-cycle fatigue conditions, but the opposite is likely to happen if the composite is deformed at high cyclic strain amplitudes, as was corroborated in several experimental studies [53,91].

5.2. *Preferential sites for crack nucleation*

The microstructural features which led to the nucleation of a fatigue crack were determined from analysis of the fracture surfaces as well as of longitudinal sections under the scanning electron microscope. These studies provided different results depending on the stress level during fatigue. A large number of microcracks was rapidly nucleated at the specimen surface from broken or decohered particles when the fatigue stress amplitude was similar to the composite yield strength [95,96], in agreement with the unit cell analyses described above [Fig. 14(b)]. These microcracks grow quickly and coalesce to form a dominant crack, which leads to specimen failure. Thus, the stiff ceramic reinforcements act as preferential sites for crack nucleation, and are ultimately responsible for the poor low-cycle fatigue properties of DRC. This is discussed in the last section of this review.

The crack nucleation mechanisms in the high-cycle fatigue regime were different. The first results were published in the late 80s or early 90s, and reported several typical sites for crack nucleation, nearly always at the specimen surface. The first were imperfections associated with cast materials, such as porosity [97,98] and large reinforcement clusters formed by particle segregation during solidification [99,100]. These defects were sometimes very large ($\gg$ 100 μm) and reduced the fatigue performance of these composites.

The second group of nucleation sites was related to the reinforcing particles. In cast composites, cracks were initiated by decohesion at the interface in materials reinforced with particles [101], whiskers [102], and short fibers [100]. In these two latter cases, debonding was always localized at the end of the whiskers and fibers,

where the interfacial stresses were greatest. This crack initiation mechanism in cast composites was attributed to the formation of weak interfaces due either to lack of complete infiltration or to excessive contact between the molten matrix and the ceramic particles (which react to form brittle second phases). On the contrary, fatigue crack initiation at the reinforcements in powder-metallurgy composites was normally due to particle fracture. These broken particles were well above the average particle size or were found in particle clusters with a high local volume fraction of reinforcement [103,104].

Finally, a large number of fatigue cracks were nucleated at large intermetallic inclusions in the matrix in all materials [99-105]. For instance, they account for 20% of the nucleation sites in [101], 33% in [104], and up to 75% in [105]. Both Bonnen et al. [104] and Myers and Chi [105] found that the intermetallic inclusions which nucleated cracks were fractured and their size was in the range 25–100 μm.

Evidently, some of these fatigue crack nucleation sites were in one way or another processing defects. This was recognized by the manufacturers, who strove to improve the interfacial strength and the homogeneous distribution of the reinforcements in cast composites, while controlling the size distribution of the reinforcements to limit the presence of coarse ceramic particles. This led to a new generation of DRC in which fatigue crack initiation was primarily associated with large intermetallic inclusions and, to a minor extent, with particle clusters [47,106–108], which were always found at the specimen surface. This location for the critical defects is in agreement with the numerical predictions of Levin and Karisson [109]. They found that the stress concentration factor for stiff inclusions was higher if they were located at the surface than when embedded in the bulk.

Chawla et al. [108] measured the size of the crack-nucleating intermetallic inclusions in a 2080 Al alloy reinforced with 10, 20, and 30% SiC particles tested at stress levels close to the fatigue limit. The average values are plotted in Fig. 15 together with the corresponding standard deviations. Interestingly, the size of the critical inclusions for crack nucleation decreased as the reinforcement volume fraction increased. The abrasive effect of the hard SiC particles, which served as comminuting media during rolling and extrusion, was probably responsible for breaking the intermetallic inclusions to smaller sizes. This study also found that the number of cycles necessary to initiate a crack was significantly lower in the composites than in the unreinforced alloy (in high cycle fatigue conditions), even if the inclusion size was similar in both materials. This was attributed to the presence of the stiff ceramic particles, which share more of the applied load, reducing the stresses acting on the intermetallic inclusions in the composite. This also explains why the homogeneous damage-discussed in Section 5.1. was concentrated at the ceramic reinforcements while the intermetallic inclusions dispersed in the matrix were not fractured [Fig. 14(a)].

Fig. 15 also indicates that inclusions, particle clusters or defects of over 50 μm were likely to nucleate fatigue cracks under high-cycle fatigue and thus control the fatigue limit. This is in broad agreement with the data from various Al- and Mg-matrix DRC [97–100,103–107] and shows that cracks induced by fracture or decohesion of ceramic particles or intermetallic inclusions below 20 μm are not

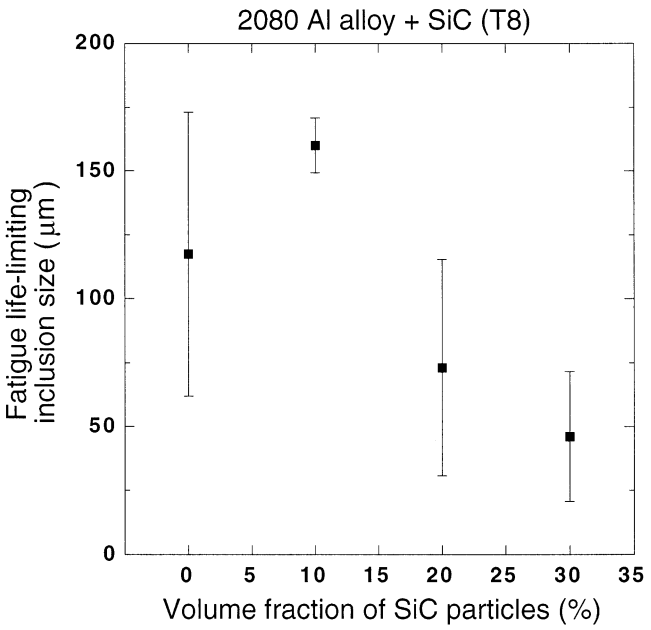

Fig. 15. Average size of the intermetallic inclusions which nucleated fatigue cracks in a 2080 Al alloy reinforced with different volume fractions of SiC particles. The bars stand for the standard deviation of the inclusion size [108].

likely to nucleate cracks in the high-cycle fatigue regime. Thus improvements in the fatigue limit by using finer reinforcements (below this limit) cannot be justified by assuming that smaller particles delay the nucleation of fatigue cracks.

Intermetallic inclusions are often responsible for fatigue crack initiation in commercial Al alloys, steels and Ni-based superalloys [36], and no qualitative differences between the composite and the unreinforced counterparts were reported in this respect. This is not the case, however, for metallic alloys containing ordered precipitates shearable by dislocations. Strain localization occurs in these materials upon cyclic deformation, and this results in a successive increased dislocation density in the glide plane, large slip offsets on the surface or stress concentrations at the grain boundaries and at the intermetallic inclusions, and early fatigue crack initiation by either grain boundary or inclusion fracture [36,110,111]. These cracks propagate along the intense slip bands, and lead to a characteristic crystallographic crack path. The dispersion of ceramic particles in the metallic alloys induces a number of microstructural changes in the metallic matrix (enhanced dislocation density, smaller grain size, weaker texture, etc.) which promote homogeneous slip and inhibit the formation of slip bands. [46,53]. Thus fatigue crack nucleation in naturally aged and underaged DRC occurred at surface inclusions and clusters and not at slip bands [46,53].

Holes and notches are always present in structural components. The effect of notches on fatigue crack initiation in DRC was analyzed by Biner [112] in a 6061 Al

alloy reinforced with 25 vol.% SiC particles in the peak-aged and overaged conditions. Crack initiation was detected using the potential drop method when the crack has propagated 100 μm from the notch root. Tests were performed with different notches whose elastic stress concentration factors varied from 2.0 to 9.6, and surprisingly, the number of cycles to nucleate a crack was independent of the notch severity for both aging conditions. Assuming that cracks were nucleated at large inclusions or clusters, Biner justified this result by assuming that the stresses are higher at sharp notches but the volume of material subjected to the influence of the notch is smaller, which reduces the probability of finding a critical defect. Although this is a plausible hypothesis, another explanation can be found in recent tests of the notch sensitivity of DRC under monotonic deformation [113]. This question remains open and more experimental data and theoretical analyses are required.

5.3. High temperature performance

Fatigue crack nucleation at elevated temperature was characterized in a few Al-based DRC [57,60,62,105,114,115]. As at ambient temperature, cracks were sometimes initiated at intermetallic inclusions and large particle clusters [57,105,115]. Various investigations reported, however, that most of the cracks were nucleated in the matrix at high temperature, especially in regions near the reinforcement ends or sharp corners [60,62,114]. These latter findings were in agreement with the analyses of the mechanisms of homogeneous damage upon cyclic deformation. Reinforcement fracture was rare at high temperature, and most the damage was due to either decohesion at the interfaces or void nucleation and growth in the matrix near the reinforcements or at grain boundaries [60,115].

The change in fatigue crack initiation sites from intermetallic inclusions and particle clusters at ambient temperature to the matrix at elevated temperature can be explained by the matrix softening at high temperature. The load transferred from the matrix to the reinforcements and inclusions is reduced with the matrix strength, and thus the critical stress for particle or inclusion fracture is not attained [75]. The progressive accumulation of plastic strains in the matrix near the reinforcements (Fig. 11) finally leads to the nucleation and growth of voids, which may coalesce to form a macroscopic crack. The process of nucleation, growth and coalescence of voids in the composite matrix was analyzed by Llorca et al. [45] in the context of unit cell simulations using the Gurson model for the matrix. The damage patterns predicted by the numerical simulations were in qualitative agreement with the experimental results at elevated temperature.

High temperature exposure may also induce severe microstructural changes in the composite matrix. In particular, stable precipitates can be formed at the particle/interface [60]. These brittle precipitates cannot accomodate the large plastic strains in the matrix and may lead to interface fracture. In addition, the growth of the stable precipitates depletes the matrix of solute in the near-reinforcement areas, which become weaker, localize the deformation, and finally nucleate cracks. Both phenomena contribute to changing the preferential sites for crack nucleation at high

temperature from intermetallic inclusions and particle clusters to failure in the matrix near the interface.

5.4. Environmental effects

The synergistic effect of cyclic loading and a corrosive environment is known to degrade the fatigue performance of metals [36]. While the corrosion of DRC is outside the scope of this paper (the reader is referred to [116,117] for more information on this topic), the influence of the environment on the fatigue crack initiation susceptibility is studied in [118,119].

The recent work of Yu et al. [119] was carried on a 6061 Al alloy reinforced with different volume fractions of either SiC particles or whiskers. It showed that the crack nucleation resistance of the composites and of the unreinforced counterpart was significantly reduced in a 3% NaC1 aqueous solution as compared to laboratory air. No differences were observed, however, between laboratory air and ion-exchanged water. The fractographic study revealed multiple crack initiation sites in each specimen tested in salt water, as opposed to those fatigued in air. They were associated with pits nucleated at the reinforcement/matrix interface and at the grain boundaries. The number of pits and their size increased with the number of fatigue cycles, and adjacent pits coalesced to form bigger ones, from which fatigue cracks grew. The preferential site for crack nucleation changed from large particle clusters (in air) to corrosion pits in salt water and this greatly reduced the fatigue limit and the high-cycle fatigue life of the composite. Thus, the susceptibility to pit formation seemed to control the crack nucleation resistance in this study but it is evident that much more research is needed.

6. Fatigue crack propagation

The kinetics of fatigue crack propagation in metallic materials has been characterized since the early 1960s through the stress intensity factor amplitude, $\Delta K = K_{\max} - K_{\min}$ which stands for the variation in the stress intensity factor at the crack tip as the load goes from maximum to minimum in each loading cycle [36]. Paris et al. [120] showed that the crack increment in each fatigue cycle, $\mathrm{d}a/\mathrm{d}N$, could be related to the stress intensity factor amplitude by the power law relationship,

$$\frac{\mathrm{d}a}{\mathrm{d}N} = A[\Delta K]^m \tag{3}$$

where A and m are constants which can be determined for a given material and environment using a standard experimental procedure [121]. Further studies demonstrated that the relationship between the crack growth rate and ΔK was better represented by an S-shaped curve (in logarithmic coordinates), where three different regions may be distinguished (Fig. 16). Eq. (3) was valid in the central region, which covered crack growth rates in the range 10^{-9}–10^{-7} m/cycle. There was, how-